Nanoscale

PAPER

View Article Online
View Journal

Cite this: DOI: 10.1039/d5nr05064b

AI-guided design of self-assembled flavonoid-cisplatin nanoparticles enhances triple-negative breast cancer therapy *via* three cell-death pathways

MarMar Tuohan,[a,b] Geng Hu,[c] Di Zhu,[d] Bo Hu,[a,b] Mengyue Ni,[a,b] Liujia Chan,[a,b] Yu Lu*[a,b] and Yuji Wang *[a,b]

Triple-negative breast cancer (TNBC) remains challenging to treat because of its aggressiveness and poor response to chemotherapy. Although cisplatin is clinically used for TNBC, its therapeutic window is narrow due to severe systemic toxicity and rapid development of drug resistance, underscoring the need for new strategies. To address this, we developed LMCDPS, a molecular language-model platform that learns the structural grammar of natural compounds, predicts their compatibility for co-assembly with cisplatin, and uniquely traces active small molecules back to their botanical origins. Using LMCDPS, we identified persimmon leaf-derived flavonoids as optimal cisplatin partners and confirmed their ability to spontaneously form stable, excipient-free nanoparticles (PLF-Cis NPs) *via* π–π interaction and hydrogen bonding. These nanoparticles eliminate synthetic carriers, reduce impurities in crude extracts, and substantially enhance tumor delivery, achieving an 11.3-fold increase in intracellular platinum accumulation. PLF-Cis NPs exert potent anti-TNBC activity by coordinating cisplatin-induced apoptosis, flavonoid-mediated ferroptosis, and immunogenic cell death, thereby promoting dendritic-cell maturation and robust $CD8^+$ T-cell infiltration. In an orthotopic 4T1 model, they achieved a 71.5% reduction in tumor growth. This study establishes a language-model-driven framework for designing natural product-based, excipient-free nanomedicines, offering a scalable path to enhance chemotherapy while mitigating systemic toxicity.

Received 1st December 2025,
Accepted 3rd May 2026

DOI: 10.1039/d5nr05064b

rsc.li/nanoscale

Introduction

Triple-negative breast cancer (TNBC), characterized by the absence of estrogen receptor (ER), progesterone receptor (PR), and human epidermal growth factor receptor 2 (HER2) expression, is unresponsive to endocrine therapy and HER2-targeted treatments. These features contribute to its highly aggressive behavior, increased likelihood of recurrence, and poor clinical prognosis.[1] Chemotherapy remains the cornerstone of systemic treatment for TNBC patients.[2] Among chemotherapeutic agents, cisplatin—a classical DNA-damaging drug—has demonstrated substantial efficacy.[3–5] However, its therapeutic performance is severely limited by two major challenges: (1) the immunosuppressive tumor microenvironment (TME) and low drug uptake efficiency, resulting in suboptimal responses to monotherapy; (2) the development of severe systemic toxicity and drug resistance, hindering its long-term application.[6,7] These limitations urgently call for synergistic strategies capable of enhancing cisplatin sensitivity while reducing adverse effects.

Nanodrug delivery systems (NDDS) offer a promising approach to overcome these limitations of cisplatin.[8–11] Beyond synthetic nanocarriers like liposomes and polymer micelles, the self-assembly of natural bioactive compounds with therapeutic agents into nano formulations has garnered considerable interest in recent years.[12,13] This approach is favored for its excellent biocompatibility and straightforward preparation methods.[14–18] For example, epigallocatechin gallate (EGCG) can coordinate with cisplatin to form stable

[a]*Department of Medicinal Chemistry, College of Pharmaceutical Sciences of Capital Medical University, Beijing 100069, P. R. China. E-mail: luyu@mail.ccmu.edu.cn, wangyuji@ccmu.edu.cn; Tel: +86 15001294280*
[b]*Beijing Key Laboratory of Intelligent Clinical Data and AI Model-driven Innovative Drug Development; Beijing Key Laboratory of Drug Innovation for Neuro-Oncology, Beijing Engineering Research Center of Targeted Drugs and Cell Therapy for CNS Tumors, Laboratory for Clinical Medicine, Capital Medical University, Beijing 100069, P. R. China*
[c]*School of Engineering Medicine of Beihang University and National Industry Education Integration Platform (Medical Engineering Cross), Beihang University, Beijing 100191, China*
[d]*Department of Pharmacy, Xuanwu Hospital of Capital Medical University, Beijing, 100053, P. R. China*

nanoparticles, thereby significantly improving tumor targeting and therapeutic efficacy.[19] However, screening vast natural product libraries to identify effective cisplatin synergists is highly challenging. Therefore, utilizing artificial intelligence presents an attractive strategy.

Artificial intelligence (AI), particularly machine learning (ML) approaches, has been widely applied across biomedical research, and has become a powerful tool for high-throughput screening and rational molecular design in drug discovery.[20,21] In nanomedicine, AI has already been applied to essential tasks including the characterization of drug delivery processes and prediction of nanodrug targeting efficiency.[22,23] Molecular language models further extend these capabilities by encoding structural and chemical features into high-dimensional representations, enabling rapid prediction of synergistic activity, self-assembly potential, and drug-like properties.[23] Compared with traditional machine-learning methods, they provide faster and more generalizable exploration across vast natural-product chemical spaces. Despite these advantages, relying on an AI-identified single compound may not fully capture the therapeutic potential of natural extracts. Experimental attempts to reconstruct extracts by mixing their major constituents at native ratios frequently fail to reproduce the full biological efficacy.[24] This suggests that synergistic interactions among multiple components contribute significantly to the superior activity of whole plant extracts.[25,26] Current AI tools virtually none support tracing an active single molecule back to its botanical origin. Such traceability would greatly facilitate reconstructing multi-component natural extracts and identifying plant sources enriched in key pharmacophores—an essential step toward bridging single-molecule predictions with the holistic properties of natural medicines.

To address these limitations, we developed a molecular language model-based computational platform, LMCDPS. This platform encodes 2D/3D molecular structures into unified tokens, enabling the simultaneous assessment of both the self-assembly potential with cisplatin and the synergistic bioactivity of natural compounds. Notably, LMCDPS introduces a reverse traceability module capable of identifying the natural sources of predicted synergists, thereby establishing a "function-oriented, source-traceable" development pipeline. Our research strategy follows a rational progression from reductionism to holism: initially, constrained by self-assembly feasibility, key pharmacophores, and mechanistic foundations, LMCDPS identified flavonoids with high synergistic potential for cisplatin. As a valuable source of flavonoids, persimmon leaves were top-ranked in our traceability model. Persimmon leaves (*Diospyros kaki* L.) have a long history of use in traditional Chinese medicine for clinical treatment of cancer and stroke-related syndromes.[27,28] Thereafter, molecular dynamics simulations investigated their multi-component co-assembly into more stable nanostructures, mimicking the complex behavior of natural extracts. Leveraging this prediction, we successfully prepared self-assembled persimmon leaf flavonoid/cisplatin nanoparticles (PLF-Cis NPs), whose combined flavonoid multimodal activity and nanoparticle-mediated tumor accumulation hold substantial promise for improving TNBC treatment outcomes.

Materials and methods

Reagents and instruments

Persimmon (*Diospyros kaki* L.) leaves are derived from fresh persimmon leaves in Anhui Province. Grade LC acetonitrile and formic acid were provided by Fisher Scientific and the ultrapure water was bought from Watsons. CQ, Fer-1, Nec-1, v-ZAD-fmk, and Methyl thiazolyl tetrazolium (MTT) were acquired from Aladdin Reagent (Shanghai, China). Dimethyl sulfoxide (DMSO) and 2′,7′-dichlorofluorescein diacetate (DCFH-DA) were obtained from Sigma-Aldrich and Fisher (USA). PBS (KGB5001), DMEM medium (KGM31800), 0.25% trypsin-EDTA digestive fluid (KGY0012) were purchased from KeyGEN BioTECH (Jiangsu, China). PBST (P1031), 4% polyformaldehyde (P1110), 5% BSA blocking solution (SW3015) were purchased from Solarbio (Beijing, China). Anti-fluorescence quenching sequester (P0126), DAPI (C1006), reactive oxygen species detection kit (S0033M), and mouse adenosine triphosphate (ATP) ELISA kit (S0026) were purchased from Beyotime (Jiangsu, China). Rabbit monoclonal [EPR3507] to HMGB1 (ab79823), Alexa fluor®488 rabbit monoclonal [EPR3924] to Calreticulin-ER marker (ab196158) were obtained from Abcam (English). Anti-CD11c-FITC (561045), anti-CD80-APC (560016), anti-CD86-PE (561963), anti-CD45-prep5.5 (561047), anti-CD8a-BV510 (563068), anti-CD3-BV421 (562600), anti-CD4-RB780 (568694) antibodies were purchased from BD Biosciences. 4T1 (mouse breast carcinoma cells), 4T1-Luc (mouse breast carcinoma cells transduction with luciferase gene) were purchased from KeyGEN BioTECH. The experimental animal BALB/c female mice were bought from Beijing Vital River Laboratory Animal Technology Co., Ltd.

Architecture and workflow of the LMCDPS platform

To systematically discover multi-component natural products that synergize with chemotherapeutic agents, we developed the LMCDPS platform, whose core innovation lies in its "Function-oriented Reverse Sourcing" capability. LMCDPS integrates dual-task molecular evaluation with a reverse mapping module that links predicted active molecules to their corresponding natural product sources based on structural and database-level associations. This design enables source-level prioritization of candidate compounds for experimental validation. Interpretability derives from function-source linkage, and scalability from unified representations enabling efficient large-scale screening without architectural changes.

As shown in Fig. 1, its workflow is logically divided into four layers:

Layer 4: knowledge base layer

This layer serves as the data foundation, integrating multiple large-scale public databases (DRUGBANK and TCMBANK) and literature to construct a comprehensive multi-dimensional knowledge base containing 2D/3D structural information,

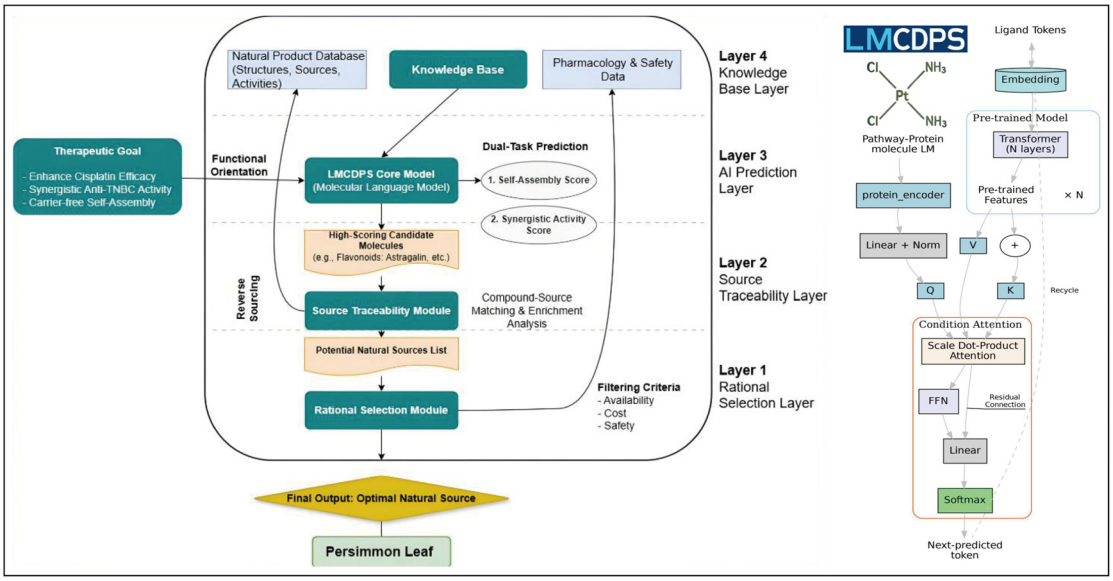

Fig. 1 LMCDPS Platform: centered on a function-oriented reverse traceability strategy for natural medicine raw materials, leveraging a transformer-based framework that integrates pathway-protein language modeling and ligand token encoding for combination prediction.

natural sources, and reported biological activities of thousands of natural compounds. All botanical source annotations in the knowledge base are supported by published phytochemical experimental studies.

Layer 3: AI prediction layer

This is the intelligent core of the platform. We deployed a Transformer-based molecular language model trained for dual-task prediction: (a) evaluating the self-assembly potential between natural compounds and cisplatin, outputting a "Self-Assembly Score"; (b) assessing the potential for synergistic bioactivity (*e.g.*, inducing ferroptosis, immunogenic cell death) in specific disease models like TNBC, outputting a "Synergistic Activity Score".

Layer 2: source traceability layer

This key innovation module enables "reverse development". It receives the list of high-scoring candidate molecules from the AI prediction layer and performs reverse queries against the knowledge base. Using an enrichment analysis algorithm, it identifies which natural raw materials are highly enriched with these functionally ideal candidate molecules, generating a prioritized "Potential Natural Source List". Notably, this traceability step is based on compound-source annotations from curated databases and is used to quickly narrow down potential natural sources rather than to experimentally verify compound origins.

Layer 1: rational selection layer

This final decision-making layer introduces real-world constraints. It comprehensively evaluates the "Potential Natural Source List" using pharmacological safety data from the knowledge base, combined with external criteria such as availability, extraction cost, and existing research foundation, ultimately recommending the most promising candidate raw material.

Core technical modules

The Language Model-based Combination Drug Prediction System (LMCDPS) core is built upon the Token-Mol paradigm and shares the same core code framework with our previously reported related studies.[22] The model has been previously benchmarked against conventional methods and demonstrated robust performance. In this study, LMCDPS is applied to prioritize candidate combinations for experimental validation based on the learned representations.

Input encoding and model architecture

LMCDPS establishes a multi-input, condition-aware predictive framework through the unified encoding of candidate ligands, cisplatin, and biological context such as pathway-protein associations. Each input is tokenized to represent both two-dimensional molecular structures (*e.g.* SMILES strings) and three-dimensional conformational features, including torsion angles, interatomic distances, and bond angles.

Inspired by the multimodal embedding strategies of Token-Mol, our approach integrates geometric descriptors with molecular semantics into a discrete sequence of embedded tokens, effectively capturing both structural and functional information. This representation can be formally expressed as:

$$T_{\text{ligand}} = \text{tokenize}_{\text{Mol}}(S_{2D}, G_{3D})$$

Pathway-protein contextual information is incorporated in the form of "pathway context", and is processed *via* a dedicated Protein Encoder module to capture pathway and target-specific features, formally defined as:

$$\begin{aligned} T_{\text{ligand}} &= \text{tokenize}_{\text{Mol}}(S_{2D}, G_{3D}) E_{\text{pathway}} \\ &= \text{encoder}_{\text{Prot}}(P_{\text{seq}}, \text{pathway}_{\text{ID}}) \end{aligned}$$

All input representations are first processed through linear projection layers followed by LayerNorm normalization, before being integrated into the core Transformer architecture.

Pretraining and conditional attention mechanism

The core of LMCDPS is implemented using an *N*-layer Transformer decoder architecture, consistent with the TokenMol framework. It adopts an autoregressive modeling strategy, incorporating causal masking to emulate the sequential nature of token generation. The training objective is to maximize the likelihood of accurately predicting the next token in the sequence, formally expressed as:

$$\mathcal{L}_{\mathrm{LM}} = -\sum_{t=1}^{T} \log P(x_t | x_{<t}, C)$$

Here, C denotes the conditional inputs, encompassing both the molecular structure of cisplatin and the pathway context, while x_t represents the t-th output token in the sequence.

Multi-objective prediction and scoring mechanism

For each cisplatin–candidate compound pair, the model generates a sequence of output tokens, which is subsequently processed by a *post hoc* module to extract predicted scores across multiple biological endpoints—including breast cancer relevance, apoptotic activation, and immune response. Target-specific scoring is achieved *via* a multi-head linear projection layer, defined as:

$$s_i = \mathrm{MLP}_i(H), \quad i = 1, \ldots, K$$

Here, H represents the hidden states produced by the Transformer, and K denotes the number of biological target dimensions—such as breast cancer-specific targets and drug assembly potential. Each score $s \in [0, 1]$ reflects the model's confidence with respect to the corresponding objective.

Preparation of PLF-Cis NPs

PLF and cisplatin were separately dissolved in DMSO at a feeding mass ratio of 10 : 1. PLF (1.8 mg mL^{-1}) was mixed with cisplatin at 1 : 1 (v/v) and then added dropwise to water at 1 : 5 (v/v). Nanoparticles were then subjected to ultrasonication (power: 400 W, duration: 10 min, temperature: 25 °C) to facilitate dispersion and accelerate the self-assembly process. After formation, the suspension was purified using 30 kDa ultrafiltration centrifugation. For biological experiments, the nanoparticle suspension was sterilized by filtration through a 0.22 μm sterile membrane to eliminate potential microbial contamination. The encapsulation efficiency and drug loading capacity of PLF were determined by ultraviolet-visible (UV-Vis) spectrophotometry at the characteristic absorption band of flavonoids using a PLF-equivalent reference standard, while those of cisplatin were measured using ICP-MS.

Intracellular GSH or MDA level detection

4T1 cells were seeded and incubated in 6-well plates at a density of 1×10^5 cells per well for 24 h, followed by treatment with cisplatin, PLF and PLF-Cis NPs, respectively. Cells were harvested, and the intracellular GSH or MDA content was assessed using a reduced GSH or MDA assay kit. The final content of intracellular GSH was expressed as nanomoles of GSH per 10^6 cells.

Intracellular lipid peroxides (LPO) levels level assay

Intracellular lipid peroxides were detected *via* C11-BODIPY$^{581/591}$ following manufacturers' instructions: 4T1 cells were seeded and incubated in confocal cell culture dishes for 24 h, followed by treatment with PBS, cisplatin and PLF-Cis NPs for an additional 24 h. Olympus fluorescence microscope and flow cytometer (BD LSR Fortessa Cell Analyzer) was used to detect the fluorescence.

ICD induction *in vitro*

4T1 cells were exposed to the indicated concentrations of the test compound in confocal dishes for a duration of 24 h. Following this incubation period, the cells were fixed using methanol, permeabilized with 0.1% Triton X-100, and blocked with goat serum at room temperature for 0.5 h. Subsequently, the cells were incubated with primary antibody overnight at 4 °C, followed by incubation with a secondary antibody at room temperature for 1 h in a dark environment. DAPI was employed for staining the cell nuclei, and the cells were then imaged using a Carl Zeiss STED confocal fluorescence microscope.

Furthermore, the secretion of HMGB1 and ATP was evaluated by treating 4T1 cells in a similar manner. ATP release was measured at a sub-IC_{50} concentration of 2 μM, under which cell viability remained relatively high, ensuring that the observed extracellular ATP primarily reflects regulated immunogenic cell death (ICD) rather than non-specific cell lysis. Upon incubation, the supernatant was collected and analyzed using ELISA kit protocols.

Single-cell mass cytometry (Cy-TOF)

Fresh tumor tissues were prepared into single-cell suspensions using type IV collagenase and DNase. Live cells were isolated and fixed with FIX I (Fluidigm, CA, USA) solution for 15 min. The cells were stained with antibodies to surface markers with metal markers for 30 min, then infiltrated with Perm-S (Fluidigm, CA, USA), and stained with antibodies to intracellular markers and washed three times. After treating with iridium-containing DNA intermediates (191 Ir/193 Ir, final concentration 125 nM) in FIX and Perm (Fluidigm, CA, USA) solutions at room temperature for 1 h, they were re-suspended in 10% EQ 4 element calibration beads (Fluidigm, CA, USA) solution and then detected on Helios flow mass spectrometry (Fluidigm, CA, USA). Data were analyzed using the gating strategy detailed in Fig. S12.

In vivo antitumor immunity

Female BALB/c mice were purchased from Beijing Vital River Laboratory Animal Technology Co., Ltd. All animal experiments were executed according to the protocols approved by

the institutional animal care and use committee of Capital Medical University; the ethics number is AEEI-2024-341. The animals received humane care.

1×10^6 4T1-luc tumor cells per mouse were injected into the third breast pad of BALB/c mice. When the size of the tumor reached 75–100 mm^3, all animals were randomly assigned to different groups (8 mice per group) using a random number table, and allocation concealment was applied during grouping and treatment to avoid selection bias. Sample size was determined based on comparable literature reports, preliminary experiments, and the 3R guidelines for animal research. The groups were intravenously injected with normal saline; cisplatin (1 mg kg^{-1}); cisplatin (2 mg kg^{-1}); PLF-Cis NPs-high (1 mg kg^{-1}); PLF-Cis NPs-medium (0.4 mg kg^{-1}); PLF-Cis NPs-low (0.1 mg kg^{-1}) every two days, respectively. Normal saline was used as a negative control, while free cisplatin served as a clinically relevant reference. This dosing schedule was chosen to balance the pharmacological characteristics of cisplatin-based nanoparticles with the rapid progression of the 4T1 orthotopic breast tumor model, and is consistent with previously reported treatment regimens in similar 4T1 studies.[29,30] The formula used to calculate tumor volume was (1/2 × length × width × width), where the length was determined by the long axis diameter and the width was determined by the short axis diameter. In addition, all outcome assessments, including body weight monitoring, tumor volume measurement, and histological evaluation, were performed in a blinded manner by investigators who were unaware of the group assignments. After the mice were sacrificed on the 22th day, the tumor tissue and major organs were harvested and weighed, and then frozen in liquid nitrogen or fixed in formalin for further use. For histopathological analysis and immunohistochemistry, the major organs and tumors were fixed with 4% paraformaldehyde, and subsequently dehydrated and embedded in paraffin. After dewaxing and rehydrating, 2 μm-thick sections were prepared and treated with hematoxylin and eosin (H&E) for routine examination. In terms of immunohistochemistry analysis, 4 μm-thick sections were prepared, and then blocked and permeabilized in 2% BSA and 0.2% Triton X-100 in PBS at 25 °C for 20 min. The staining was conducted using the indicated combination of primary antibodies at 4 °C overnight, followed by treatment with secondary antibody (Alexa Fluor®568) for 1 h and DAPI for 5 min away from light. The sections were imaged by a section scanner (Pannoramic MIDI, 3DHISTECH, Hungary) and analysis by Image J. Serum ALT, AST, UREA, CREA-S were measured with the corresponding kits by an automatic biochemical analyzer (BS-600, mindray). Complete blood counts were analyzed by an automatic blood cell analyzer (URIT-5160Vet, mindray).

The tumor-bearing mice were intraperitoneally injected with 0.1 mL of D-luciferin potassium salt (10 mg mL^{-1}) at the 1st day and 15th day of administration. The mice were anesthetized with isoflurane 10 min after injection, then the fluorescence signals were obtained by the IVIS spectral system, and the data were processed and analyzed using Living Image 4.4.

To examine the immune response, tumors were obtained from the tumor-bearing mice and prepared into a single-cell suspension. The cells were then labeled with anti-CD11c-FITC, anti-CD80-APC, anti-CD86-PE, anti-CD45-prep5.5, anti-CD8a-BV510, anti-CD3-BV421, anti-CD4-RB780 antibodies, and analyzed by flow cytometry.

Statistical analysis

All experiments were performed with at least three independent biological replicates unless otherwise stated. Key findings were further validated in independent experiments to ensure reproducibility. Data are expressed as mean ± standard deviation (SD). Statistical analysis was performed using GraphPad Prism 8.0.

Normality test and homogeneity of variance test were performed before one-way ANOVA. Differences among multiple groups were evaluated by one-way ANOVA followed by Tukey's *post hoc* test. * Indicates $p < 0.05$, ** indicates $p < 0.01$ and *** indicates $p < 0.001$ were considered statistically significant.

Results

LMCDPS validation and screening output

The core architecture of the LMCDPS platform, which integrates both 2D/3D molecular features and biological context for combination therapy prediction, is depicted in Fig. 1. This framework enabled efficient screening of candidate compounds from curated databases such as DrugBank and TCMBank (Fig. 2a), providing a robust foundation for the subsequent identification of synergistic partners for cisplatin. The platform's effectiveness was validated by defining the therapeutic goal: identifying a multi-component natural extract capable of self-assembling with cisplatin into a carrier-free nanodrug and synergistically enhancing its efficacy against TNBC.

(i) Functional definition & AI virtual screening: the AI prediction layer screened the vast compound library. Results indicated that molecules excelling in both "Self-Assembly Score" and "Synergistic Activity Score" predominantly shared a flavonoid backbone. The multi-objective prediction scores for different natural products combined with cisplatin across key targets (breast cancer, apoptosis, immune regulation, drug assembly) are presented in Fig. 2b. Among the top 12 compounds selected from the 70 000-compound library, 5 were flavonoids.

(ii) Reverse traceability & source enrichment analysis: the source traceability layer, operating on the high-scoring flavonoid list, identified several plants containing these compounds. Persimmon leaves (*Diospyros kaki* L.) showed significant enrichment advantages in both the variety and relative content of the target active ingredients (Fig. 2c).

(iii) Rational decision & final source determination: the rational selection layer evaluated the traceability results. Considering the wide availability, low cost, mature extraction techniques, and established safety profile of persimmon

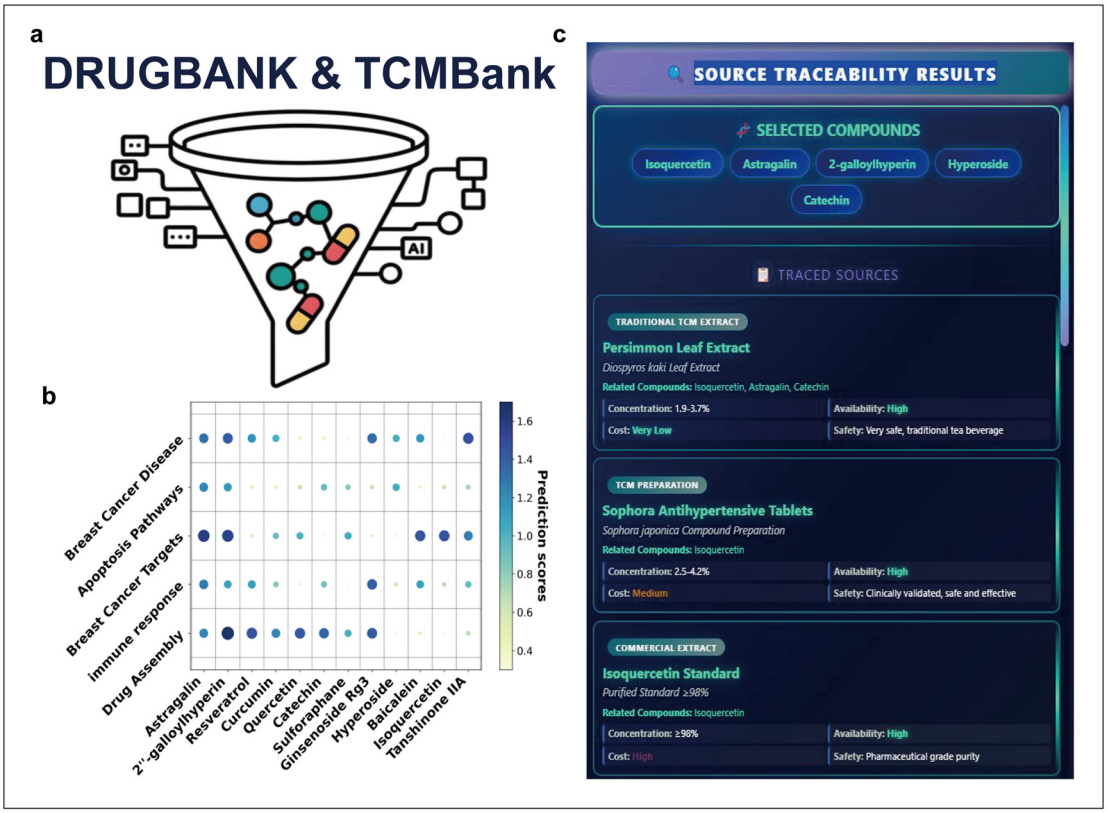

Fig. 2 Architecture of the LMCDPS molecular language model for synergistic drug combination screening and function-oriented reverse sourcing. (a) Screening pipeline for identifying potential drug candidates from natural product databases (*e.g.*, TCMBank). (b) Multi-objective prediction scores of natural products (*e.g.*, astragalin) combined with cisplatin across key targets including breast cancer, apoptosis, immune response, and drug assembly. (c) Source traceability results.

leaves, the platform conclusively designated persimmon leaf as the optimal natural source for subsequent experimental studies.

Extraction and purification of persimmon leaf flavonoids (PLF)

Based on the aforementioned screening results and a comprehensive consideration of raw material availability, extraction cost, and established pharmacological safety data, persimmon leaves were selected as the multi-component flavonoid source for subsequent investigation. As illustrated in Fig. 3a, standardized PLF were obtained through ultrasound-assisted extraction followed by macroporous resin purification.

Phytochemical characterization revealed the identification of 35 flavonoid and polyphenol compounds from PLF (Fig. 3b, c and Tables S1, S2). Quantitative analysis of 11 common flavonoids showed that the top 5 most abundant compounds were highly consistent with the flavonoids receiving the highest prediction scores from the LMCDPS model, with a combined content of 208.7 μg mL^{-1} (Fig. 3c). This result strongly validates the feasibility of our proposed research strategy, which traces potential active components back to their botanical source (persimmon leaves) through flavonoid profiling.

Furthermore, the ^{1}H-NMR spectrum of PLF confirmed the presence of characteristic signals corresponding to the flavonoid skeleton (Fig. S2). Based on the simulations and scoring of self-assembly behavior between the five flavonoids and cisplatin conducted on the LMCDPS-MD platform (Fig. 3d and e), the results indicated that the multi-component combination achieved the highest score (Fig. 3f). Therefore, we ultimately selected this multi-component system for the preparation of nanodrugs.

Self-assembly of PLF-Cis NPs

Different feeding mass ratios of PLF to cisplatin were screened, and a ratio of 10 : 1 was identified as yielding the optimal synergistic effect. This ratio was therefore adopted for the preparation of PLF-Cis NPs (Fig S3). The encapsulation efficiency and drug loading of PLF and cisplatin in PLF-Cis NPs were determined using an ultrafiltration–centrifugation method. At the feeding ratio of 10 : 1, the encapsulation efficiencies of cisplatin and relative incorporation of PLF were 78% and 83%, respectively, indicating favorable co-assembly behavior and efficient co-encapsulation. Based on the total dry weight of the nanoparticles, the drug loading of cisplatin and relative PLF content were 8.96% and 74.9%, respectively.

TEM micrographs demonstrated that PLF exhibited uniformly fine morphology (<100 nm), while cisplatin formed spherical aggregates approximately 300 nm in diameter. When

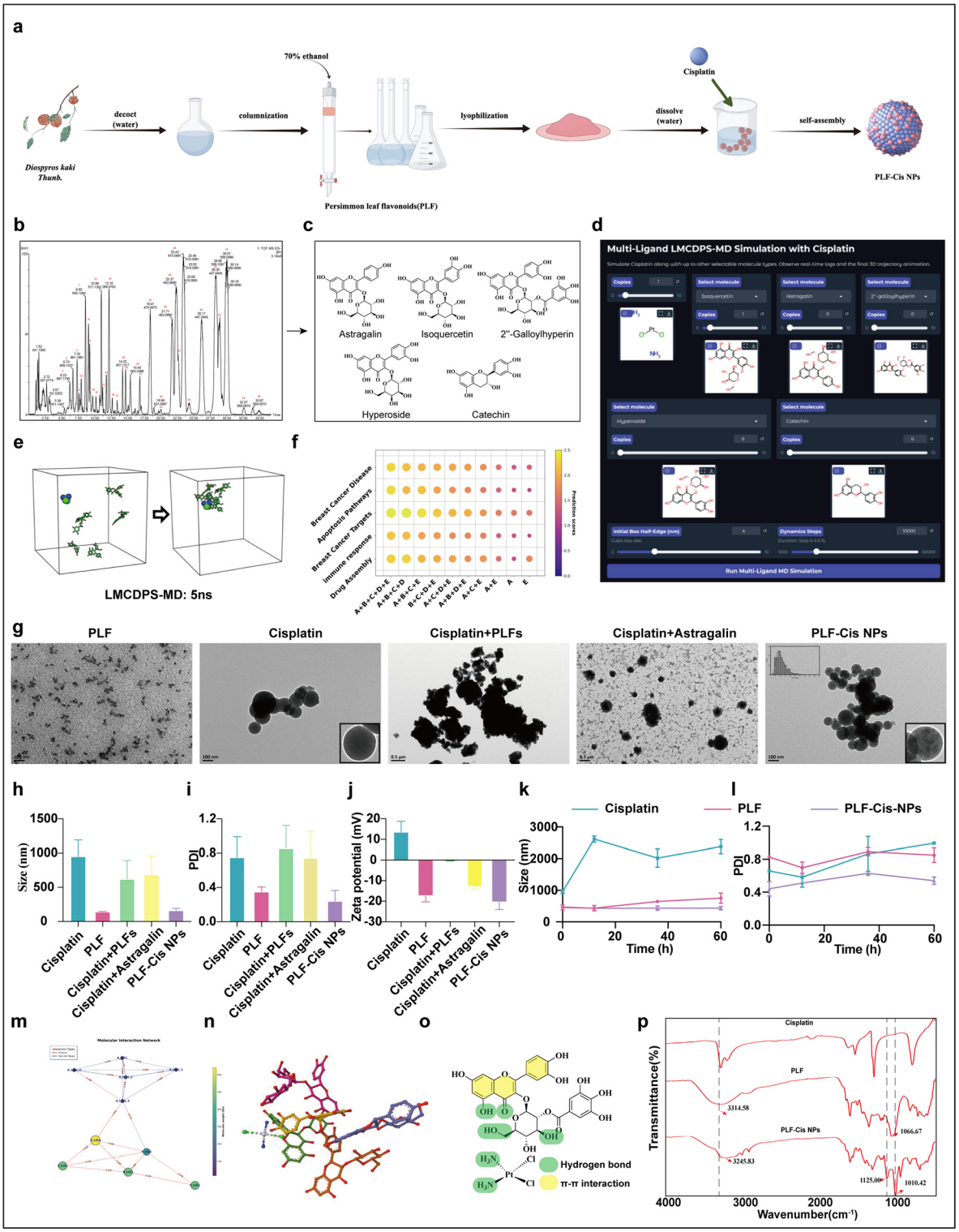

Fig. 3 Preparation and characterization of self-assembled nanoparticles. (a) Schematic of the self-assembly process. (b) LC-MS/MS chromatogram and mass spectrum of PLF. (c) Structures of the five most abundant PLF compounds. (d) Molecular dynamics simulation interface configured for studying flavonoid–cisplatin interactions. (e) Representative 3D flavonoid conformations before and after simulation. (f) Predicted synergy of multi-flavonoid combinations with cisplatin (A: Isoquercetin; B: Astragalin; C: 2''-Galloylhyperin; D: Hyperoside; E: Catechin). (g) TEM image of nanoparticles. Scale bar = 100 nm or 0.5 μm. (h–l) Nanoparticle Stability over 60 h. (m–o) Demonstration of PLF-Cis NPs Interaction Prediction. (p) FT-IR spectra of cisplatin, PLF and PLF-Cis NPs. Data are shown as mean ± SD. Artworks created with FigDraw.

cisplatin was assembled with either multi-component PLFs or single-component astragalin, irregular aggregates were produced. In contrast, multi-component PLF and cisplatin co-assembled into well-defined spherical nanoparticles (PLF-Cis NPs, 116.8 ± 35.5 nm), with fine PLF particles observed to be self-assembled and attached to their surface (Fig. 3g). Dynamic light scattering (DLS) revealed that cisplatin in aqueous solution displayed a particle size distribution centered at ~1000 nm (Fig. 3h), which is larger than the size observed by TEM. This difference arises from the distinct measurement principles of the two techniques: TEM reflects the dry-state core size, whereas DLS measures the hydrodynamic diameter in solution. Moreover, the free cisplatin dispersion exhibited a relatively high polydispersity index (PDI), indicating aggregation in aqueous environments that further increases the apparent particle size detected by DLS (Fig. 3i).

Zeta potential measurements demonstrated that the aqueous solution of cisplatin had a positive surface charge (+13.5 ± 5.3 mV), whereas the PLFs had a negative surface charge (−17.3 ± 2.9 mV). Upon electrostatic self-assembly into composite nanoparticles, the surface potential significantly decreased to −20.4 ± 3.6 mV (Fig. 3j), suggesting that initial electrostatic attraction drives primary aggregation, which is subsequently stabilized by cooperative hydrogen bonding and π–π stacking interactions within the multi-component PLF system, enabling the formation of stable nanoparticles that cannot be achieved by single flavonoid components alone. Consistent with the TEM observations, the small particles attached to cisplatin surfaces are likely formed through electrostatic adsorption between oppositely charged components. Notably, PLF-Cis NPs exhibited no significant changes in particle size or PDI during a 60 h monitoring period in both aqueous solution and DMEM medium containing 10% FBS (Fig. 3k, l and Fig. S4), indicating good colloidal stability of the nanocomposite system.

Interaction of PLF-Cis NPs

To explore the self-assembly mechanism of cis-PLF NPs, we used the LMCDPS-MD module for prediction and the FT-IR for verification. Computational interaction predictions utilizing the LMCDPS platform (Fig. 3m) reveal that the assembly of PLF-Cis NPs is primarily mediated by hydrogen bonding forces. Extended analysis indicates that intermolecular hydrogen bonding and π–π stacking interactions within PLF constituents may cooperatively facilitate the self-assembly mechanism integrating cisplatin with PLFs (Fig. 3n–o).

In the infrared (IR) spectrum of cisplatin, the vibrational modes of the N–H bonds exhibited distinct features: stretching vibration absorption peaks are observed at 3279 cm^{-1} and 3202 cm^{-1}, whereas bending vibration absorption peaks appeared at 1539 cm^{-1} and 1289 cm^{-1}, which is consistent with the vibrational characteristics of the ammonia ligands (NH_3) in cisplatin. The IR spectrum of the PLFs displayed a broad and intense absorption band near 3314 cm^{-1}, attributed to the stretching vibration of its associated hydroxyl groups (–O–H). When the two components self-assembled into a complex (PLF-Cis NPs), significant changes were observed in the IR spectrum. The –O–H stretching vibration peak of the PLFs shifted from 3314 cm^{-1} to 3245 cm^{-1} and had a narrower peak shape, indicating disruption of the hydroxyl association and weakened intramolecular hydrogen bonding. The –C–O stretching vibration peak of the secondary alcohol in the sugar moiety of the PLFs rather than the phenolic hydroxyl groups (Fig. 3p). In addition, two-dimensional nuclear Overhauser effect spectroscopy (2D-NOESY NMR, Fig. S5) was further performed to verify the intermolecular interactions. Obvious cross-peaks were observed between the NH_3 protons of cisplatin and the hydroxyl protons of the sugar moieties in PLFs, with a spatial distance of 3.5–5 Å, which is typical for intermolecular hydrogen bonding. Combined with FT-IR and molecular dynamics simulation results, these data confirm that cisplatin and PLFs form stable self-assembled nanoparticles mainly through hydrogen bonding between the NH_3 ligand of cisplatin and the sugar hydroxyl groups of PLFs, rather than phenolic hydroxyl groups.

Cell cytoxicity

PLF exhibited no cytotoxicity toward cancer cells (Fig. S6). We further evaluated the cytotoxic effects of PLFs, astragalin, and their combinations with cisplatin. The results revealed that single-component astragalin antagonized cisplatin's cytotoxic activity. The combination of five-component PLFs with cisplatin failed to demonstrate synergistic effects. In contrast, the self-assembled nanodrug PLF-Cis NPs significantly enhanced the tumoricidal activity of cisplatin in a synergistic manner (Fig. 4b and c). Notably, PLF-Cis NPs exhibited stronger cytotoxicity than the physical mixture of PLF and cisplatin at equivalent Pt concentrations, further supporting the advantage of nanoparticle assembly (Table S4). Using the Bliss independence model, we obtained $\Delta E > 0$, confirming the synergistic interaction. Further functional characterization showed that PLF-Cis NPs substantially inhibited the colony-forming capacity of tumor cells (Fig. 4d), which may be attributed to enhanced cellular internalization of the nanoparticles.

Cellular uptake

To further investigate the synergistic antitumor mechanism of PLF-Cis NPs, we utilized ICP-MS to quantify platinum uptake, comparing the nanoparticles with free cisplatin. As shown in Fig. 4e, cells treated with PLF-Cis NPs exhibited an 11.3-fold higher platinum content than those in the free cisplatin group, indicating enhanced cellular accumulation. As previously mentioned, PLF-Cis NPs may form a more stable self-assembled nano-solution with a smaller diameter, which may facilitate the enhanced cellular uptake of the drug. Pretreatment with endocytosis inhibitors did not reduce PLF-Cis NPs uptake (Fig. S7), suggesting that cellular entry is largely independent of classical pathways and primarily mediated by the nanoparticles themselves.

Anti-migratory activity

The anti-metastatic activity of the nanodrug was further evaluated using a wound healing assay. As shown in Fig. 4f and g,

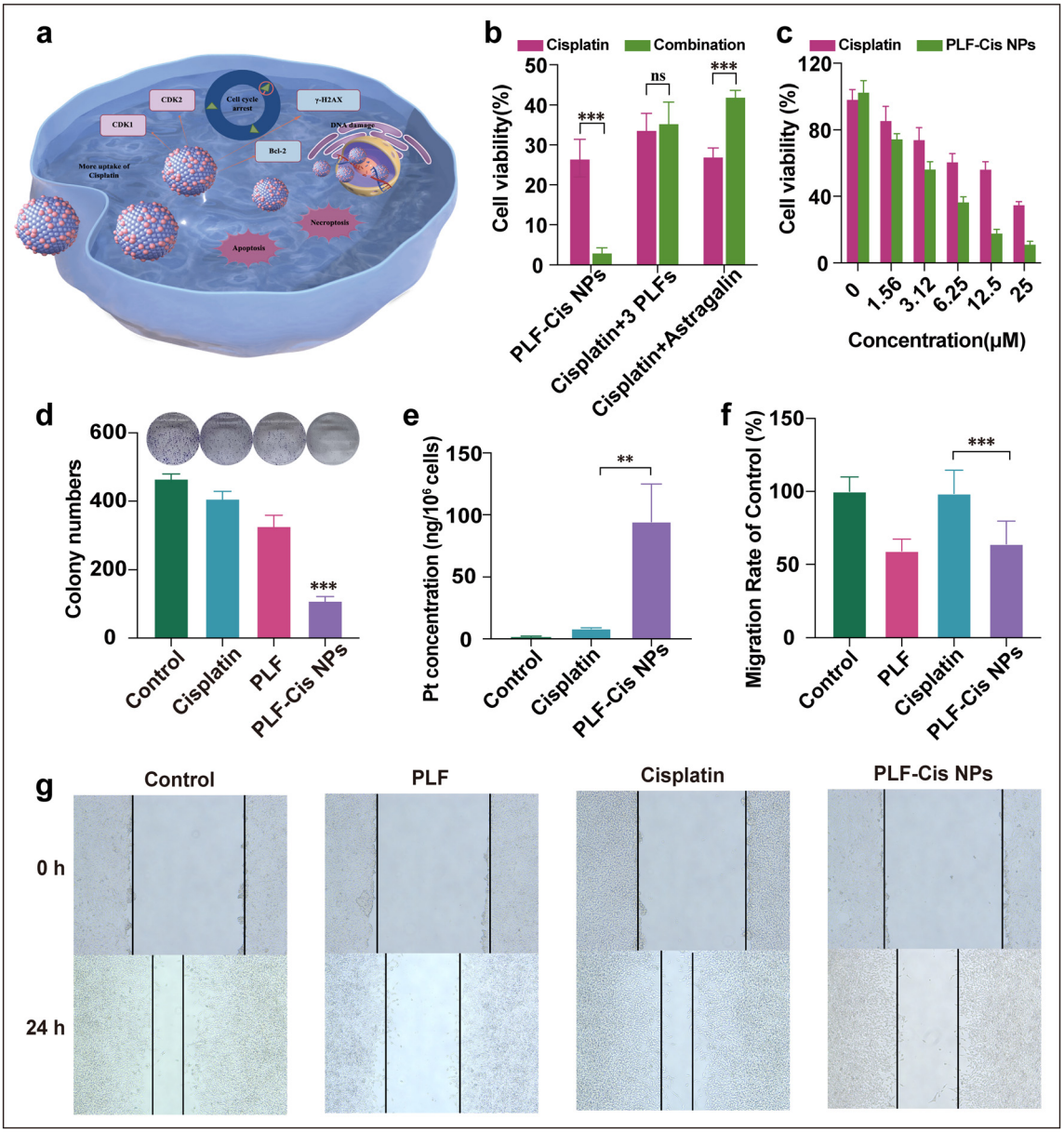

Fig. 4 *In vitro* anti-tumor and anti-metastatic activity of PLF-Cis NPs. (a) Schematic illustration of the PLF-Cis NPs-mediated synergistic anti-tumor effects. (b and c) Cell viability of 4T1 cells treated with cisplatin, cisplatin with PLF and astragalin, and PLF-Cis NPs. (d) Representative images and quantitative analysis of colony formation in 4T1 cells treated with control, PLF, cisplatin, and PLF-Cis NPs. (e) Intracellular platinum content in 4T1 cells treated with cisplatin and PLF-Cis NPs, quantified by ICP-MS. (f) Quantitative analysis of wound closure rate. (g) Representative images of the wound healing assay at 0 h and 24 h post-treatment. Data are presented as mean ± SD (n = 3). *p < 0.05, **p < 0.01, ***p < 0.001. Artworks created with FigDraw.

compared to the control and cisplatin groups, both PLF and PLF-Cis NPs significantly reduced the wound closure rate of 4T1 cells after 24 hours of treatment. This indicates that PLF-Cis NPs effectively retain the anti-metastatic activity of PLF while maintaining the cytotoxic activity of cisplatin.

Proteomic analysis reveals key pathways linked to DNA damage, cell cycle arrest and apoptosis

To decode the molecular pathways triggered by enhanced cisplatin internalization, we performed quantitative proteomic analysis of 4T1 cells treated with PLF-Cis NPs *versus* control. Gene set enrichment analysis revealed significant upregulation of key pathways including apoptosis (WP1254), DNA damage response (WP4596), and G1-to-S cell cycle control (WP413) (Fig. 5a), providing a mechanistic framework for our subsequent targeted validation.

DNA damage and cell cycle

Consistent with proteomic enrichment of cell cycle and DNA damage-related pathways, we first evaluated cell cycle distri-

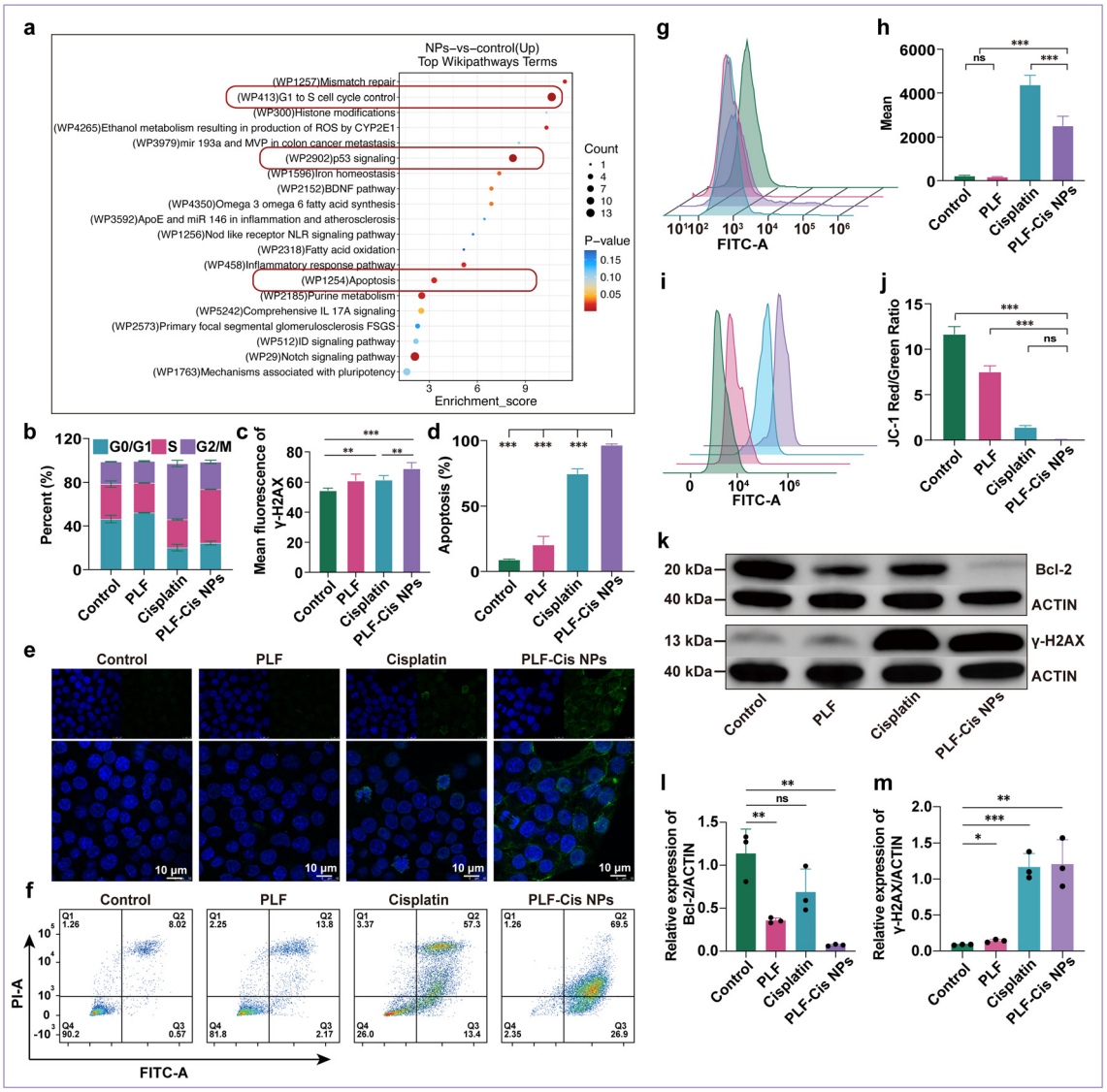

Fig. 5 DNA damage, cell cycle arrest and apoptosis induced by PLF-Cis NPs in 4T1 cells. (a) Proteomic pathway enrichment analysis of 4T1 cells treated with PLF-Cis NPs *versus* control, highlighting pathways related to apoptosis, DNA damage response and cell cycle regulation. (b) Cell cycle distribution of 4T1 cells treated with different formulations, analyzed by flow cytometry. (c) Quantitative analysis of γ-H2AX mean fluorescence intensity. (d and f) Apoptosis analysis of 4T1 cells determined by Annexin-V/PI staining and flow cytometry. (e) Confocal microscopy images of γ-H2AX foci (green) in 4T1 cells (scale bar = 10 μm). (g and h) Intracellular ROS levels in 4T1 cells measured by flow cytometry. (i and j) Mitochondrial membrane potential ($\Delta\Psi_m$) analyzed by JC-1 staining. (k–m) Western blot analysis of Bcl-2 and γ-H2AX expression in 4T1 cells, with ACTIN as the loading control. Data are presented as mean ± SD (n = 3). *p < 0.05, **p < 0.01, ***p < 0.001, ns: not significant.

bution. A greater proportion of cells in the PLF-Cis NPs group were arrested in the S phase (Fig. 5b), indicating more effective inhibition of DNA synthesis, likely attributed to increased platinum-DNA intercalation.

To assess DNA double-strand breaks, we performed confocal microscopy using γ-H2AX as a marker. Pronounced γ-H2AX foci (green fluorescence) were observed in the PLF-Cis NPs group (Fig. 5e), with significantly higher mean fluorescence intensity compared to control and free cisplatin groups (Fig. 5c). This enhanced genotoxic effect was further confirmed by western blot, which showed elevated γ-H2AX expression in PLF-Cis NPs-treated cells (Fig. 5k and m). Additionally, PLF-Cis NPs significantly downregulated the expression of cell cycle regulators CDK1/2, leading to cell cycle arrest (Fig. S7).

Cell apoptosis

The antiproliferative mechanism of cisplatin primarily involves inducing cancer cell apoptosis, which was also highlighted in our proteomic data. We examined apoptotic status *via* Annexin-V/PI flow cytometry: representative plots (Fig. 5f) and quantitative analysis (Fig. 5d) showed that PLF-Cis NPs markedly increased the proportion of apoptotic cells (Q2 + Q3 quad-

rants) compared to control, free cisplatin, and PLF-alone groups.

To dissect the apoptotic pathway, western blot analysis revealed that PLF-Cis NPs significantly reduced the expression of Bcl-2, an anti-apoptotic protein (Fig. 5k and l), suggesting activation of the mitochondrial apoptotic pathway.

Oxidative stress and mitochondrial function

To further validate the mitochondrial apoptotic mechanism, we measured intracellular ROS levels and mitochondrial membrane potential ($\Delta\Psi_m$). Flow cytometry showed that ROS levels were significantly elevated in PLF-Cis NPs-treated cells (Fig. 5g and h), leading to oxidative stress. Meanwhile, a marked loss of $\Delta\Psi_m$ was observed (Fig. 5j), consistent with Bcl-2 downregulation and mitochondrial dysfunction.

Mechanism of cell death

To systematically decode the distinct cell death patterns induced by PLF-Cis NPs compared with free cisplatin, we performed quantitative proteomic analysis and pathway enrichment. As shown in Fig. 6a, ferroptosis was identified as the top enriched pathway in PLF-Cis NPs-treated 4T1 cells relative to free cisplatin. The involvement of distinct cell death modalities was assessed using specific inhibitors: z-VAD-fmk (apoptosis), Nec-1 (necroptosis), Fer-1 (ferroptosis), and CQ (autophagy).[31] Cell viability of the cisplatin-only group was significantly restored by Nec-1 (Fig. 6b), consistent with secondary necroptosis triggered by accumulated apoptotic cells. In contrast, Fer-1, z-VAD-fmk, and Nec-1 all robustly rescued cell viability in the PLF-Cis NPs group (Fig. 6c), confirming the nanodrug exerts antitumor effects *via* a multi-modal pathway, with ferroptosis as the key driver predicted by proteomics.

Ferroptosis

To validate ferroptosis, key biomarkers of lipid peroxidation and antioxidant status were measured. Intracellular malondialdehyde (MDA), a terminal product of lipid peroxidation, was significantly elevated in the PLF-Cis NPs group compared with control and cisplatin groups (Fig. 6d). Using the peroxide-sensitive probe C11-BODIPY (581/591), flow cytometry revealed a significant decrease in red fluorescence (reduced lipids) and a corresponding increase in green fluorescence (oxidized lipids) in PLF-Cis NPs-treated cells (Fig. 6e and f). Concomitantly, intracellular glutathione (GSH) levels—critical for clearing lipid peroxides—were markedly reduced (Fig. 6g). Concomitantly, intracellular glutathione (GSH) levels —critical for clearing lipid peroxides—were markedly reduced (Fig. 6g).

Immunogenic cell death (ICD)

Beyond cisplatin, other platinum-based chemotherapeutics such as oxaliplatin are well-established inducers of ICD.[7] Emerging evidence indicates that ferroptosis can act as an immunogenic cell death modality, prompting us to assess the ICD potential of PLF-Cis NPs by measuring key damage-associated molecular patterns (DAMPs). Confocal microscopy showed pronounced cell surface exposure of calreticulin (CRT) in PLF and PLF-Cis NPs groups (Fig. 6h), with quantitative analysis confirming significantly higher CRT fluorescence intensity compared with cisplatin (Fig. 6j). For high-mobility group box 1 (HMGB1), intracellular red fluorescence intensity was markedly reduced in PLF-Cis NPs-treated cells (Fig. 6i and k), accompanied by a significant increase in extracellular HMGB1 concentration (Fig. 6l). Additionally, PLF-Cis NPs treatment led to a significant decrease in intracellular ATP levels and a concomitant increase in extracellular ATP release (Fig. 6m), a critical signal for immune cell recruitment. These results demonstrate that PLF-Cis NPs induce ICD, whereas cisplatin does not, thereby potentially enhancing antitumor immune responses (schematically illustrated in Fig. 6n).

Antitumor effects *in vivo*

To further confirm the activities and molecular mechanism of the PLF-Cis NPs *in vivo*, we evaluated their antitumor and anti-metastatic effects in an orthotopic 4T1 tumor-bearing mouse model. As shown in Fig. 7a and b, tumor volume and weight measurements indicated that high (1 mg kg^{-1}), medium (0.4 mg kg^{-1}), and low (0.1 mg kg^{-1}) dose PLF-Cis NPs groups all exhibited a significant reduction compared to the saline group. In contrast, a significant decrease was observed only in the 2 mg kg^{-1} cisplatin group, but not in the 1 mg kg^{-1} cisplatin group. Notably, the 1 mg kg^{-1} PLF-Cis NPs group (tumor growth inhibition rate = 71.5%) achieved comparable tumor inhibition to that of the 2 mg kg^{-1} cisplatin group (tumor growth inhibition rate = 61.3%). Both represented images of tumor and *in vivo* fluorescence imaging results also confirmed the superior antitumor performance of the PLF-Cis NPs (Fig. 7c–e).

Anti-metastasis effects

To assess metastatic potential, we quantified pulmonary nodules and performed a histological evaluation of lung metastases using hematoxylin and eosin (H&E) staining. Compared with control treatment, PLF-Cis NPs treatment significantly reduced both macroscopically visible and microscopic metastatic foci in lung tissues (Fig. 7f and g). These findings demonstrate that PLF-Cis NPs not only increase the antitumor activity of low-dose cisplatin but also effectively suppress tumor metastasis, suggesting their potential as a promising therapeutic strategy for TNBC treatment.

Mechanisms of action *in vivo*

ICP-MS quantitative analysis revealed that platinum accumulation in tumor tissues was significantly greater in the PLF-Cis NPs group than in the free cisplatin group. Specifically, the intra-tumoral platinum distribution rate was 8.82 ± 5.36% in the free cisplatin group, whereas that of the PLF-Cis NPs group reached 28.54 ± 8.66%, representing an approximately 3.2-fold greater accumulation efficiency (Fig. 7h). Further histopathological analysis revealed markedly increased levels of γ-H2AX (a DNA damage marker) and positive TUNEL (an apoptosis indicator) staining in tumor sections from the PLF-Cis NPs group

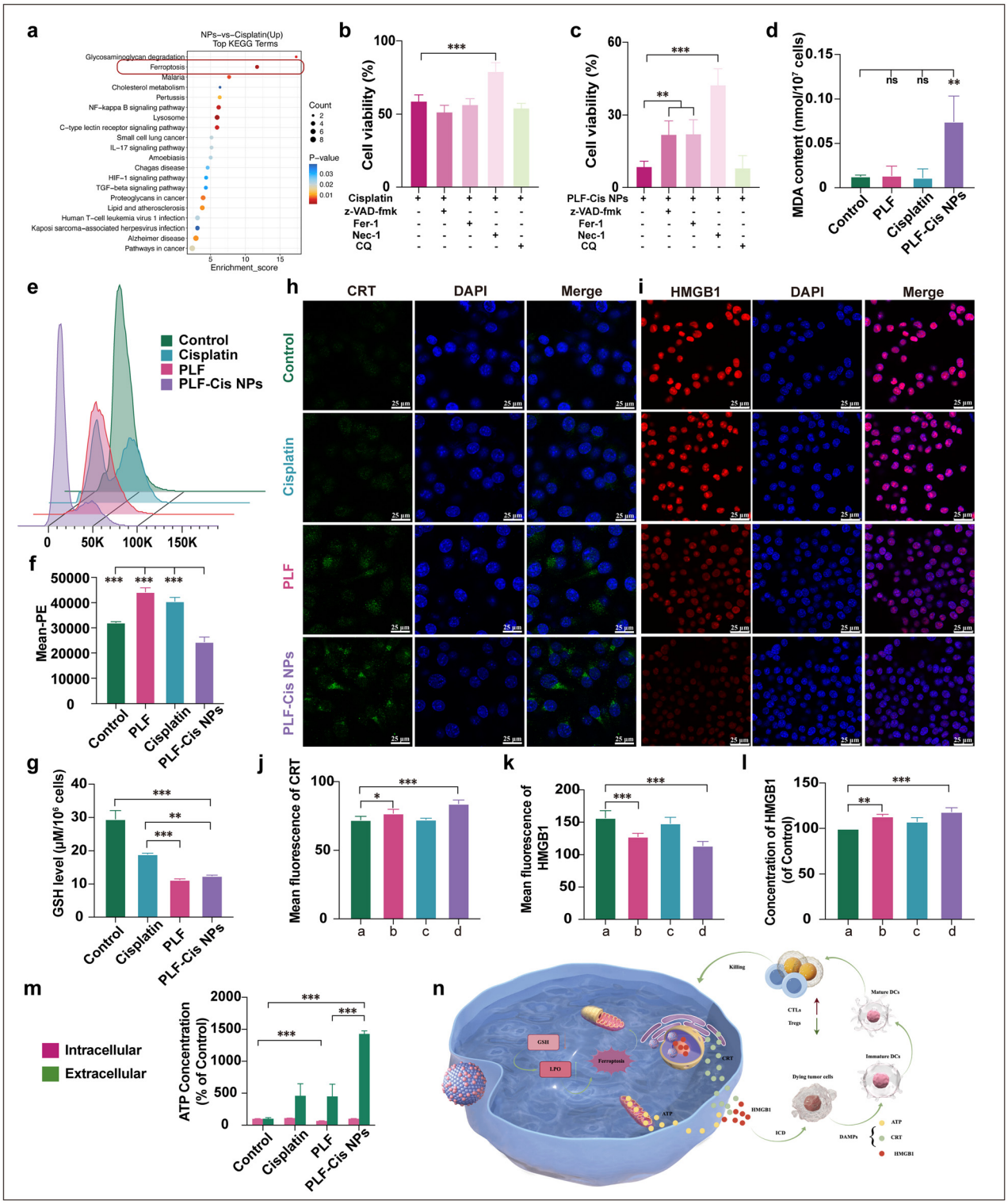

Fig. 6 PLF-Cis NPs induce ferroptosis and ICD. (a) Proteomic pathway enrichment analysis of 4T1 cells treated with PLF-Cis NPs *versus* cisplatin, highlighting pathways related to ferroptosis. (b and c) Investigation of cell death mechanisms *via* MTT assay. (d) Effect of PLF-Cis NPs on the MDA content in cells. (e and f) Flow cytometry analysis of the level of the lipid peroxidation in 4T1 cells incubated with PLF-Cis NPs. (g) Effect of PLF-Cis NPs on the GSH content in cells. (h) CLSM images depicting CRT expression. Scale bar = 25 μm. (i) CLSM images depicting HMGB1 expression. Scale bar = 25 μm. (j) Mean fluorescence intensity of CRT. (k) Mean fluorescence intensity of HMGB1. (l) The extracellular release of HMGB1 after treatment (a: control; b: PLF; c: cisplatin; d: PLF-Cis NPs). (m) Effect of PLF-Cis NPs on the intracellular and extracellular ATP content. (n) Schematic illustration of the PLF-Cis NPs-mediated ferroptosis and ICD. Data are shown as mean ± SD, $n \geq 3$, $^{*}p < 0.05$, $^{**}p < 0.01$, $^{***}p < 0.001$. ns, not significant. Artworks created with FigDraw.

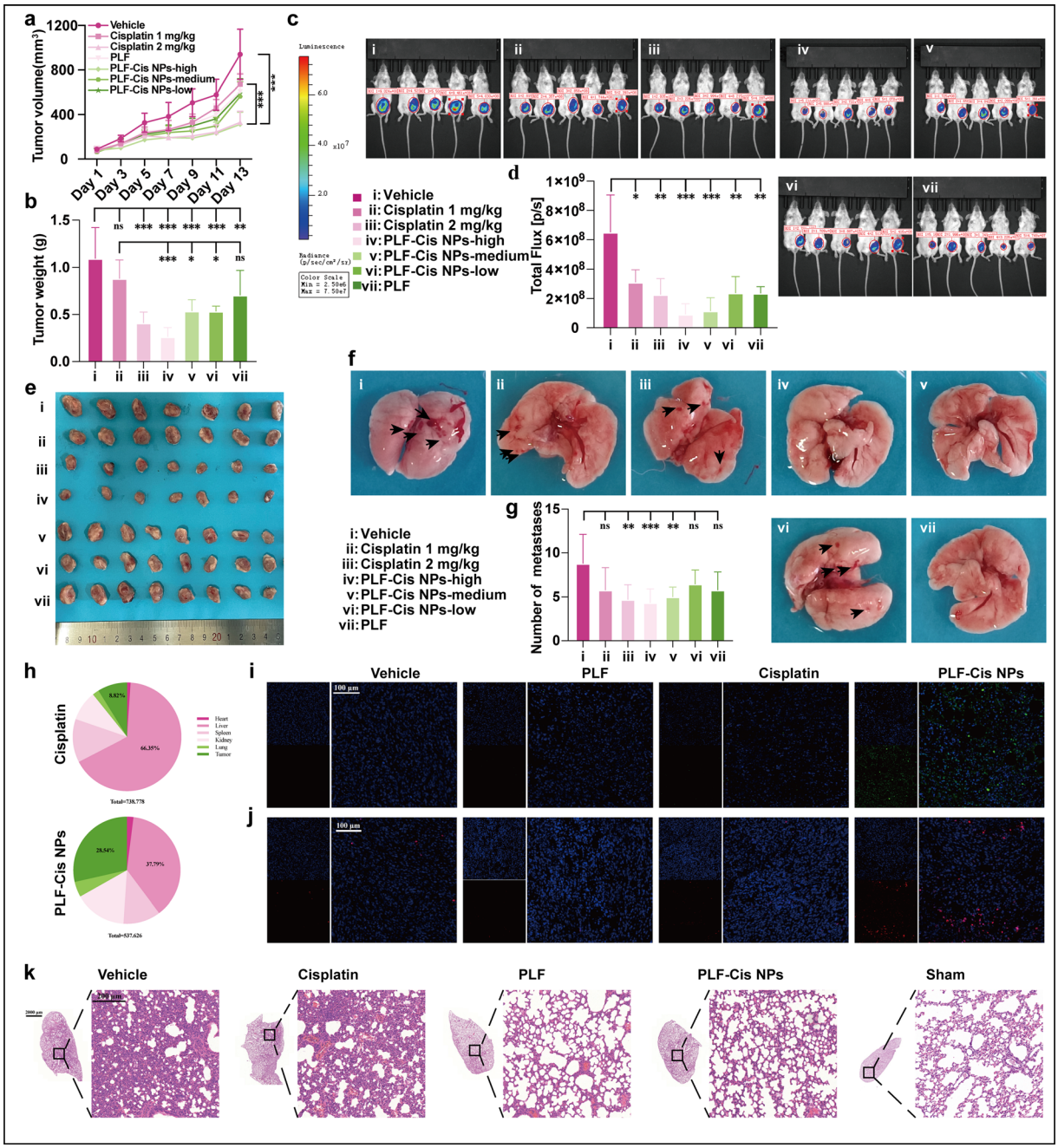

Fig. 7 Effect of PLF-Cis NPs on 4T1 orthotopic tumor-bearing mice. (a and b) Tumor volume and tumor weight of 4T1 orthotopic tumor-bearing mice (i: vehicle; ii: cisplatin 1 mg kg^{-1}; iii: cisplatin 2 mg kg^{-1}; iv: PLF-Cis NPs-high; v: PLF-Cis NPs-medium; vi: PLF-Cis NPs-low; vii: PLF). (c and d) Live animal imaging (i: vehicle; ii: cisplatin 1 mg kg^{-1}; iii: cisplatin 2 mg kg^{-1}; iv: PLF-Cis NPs-high; v: PLF-Cis NPs-medium; vi: PLF-Cis NPs-low; vii: PLF). (e) Tumors from the mice in each group (i: vehicle; ii: cisplatin 1 mg kg^{-1}; iii: cisplatin 2 mg kg^{-1}; iv: PLF-Cis NPs-high; v: PLF-Cis NPs-medium; vi: PLF-Cis NPs-low; vii: PLF). (f) Representative images of lung metastasis. (g) Number of pulmonary metastases (i: vehicle; ii: cisplatin 1 mg kg^{-1}; iii: cisplatin 2 mg kg^{-1}; iv: PLF-Cis NPs-high; v: PLF-Cis NPs-medium; vi: PLF-Cis NPs-low; vii: PLF). (h) Platinum distribution in tissues. (i) γ-H2AX expression in tumor tissue. (j) TUNEL staining of tumor tissue. Scale bar = 100 μm. (k) Representative images of HE-stained of lung tissue sections. Scale bars = 2000 or 200 μm. Data are shown as mean ± SD; $n \geq 3$, *$p < 0.05$, **$p < 0.01$, ***$p < 0.001$. ns, not significant.

(Fig. 7i and j). These results confirm that PLF-Cis NPs increase the distribution of cisplatin in the tumor sites by increasing the drug delivery efficiency, thereby increasing the degree of severe DNA damage and promoting tumor cell apoptosis.

Systemic toxicity

Given the potential systemic toxicity of platinum-based drugs, we systematically evaluated the tissue distribution profile of

platinum in PLF-Cis NPs-treated mice using ICP-MS. Analysis of the platinum-based drug distribution in organs revealed that the free cisplatin group presented significantly greater hepatic platinum accumulation (66.35 ± 2.77%), whereas the PLF-Cis NPs group presented a markedly reduced proportion of platinum accumulation in the liver (37.79 ± 10.04%) (Fig. 7h). These results indicate that the tumor-targeted delivery properties of PLF-Cis NPs substantially decreased the hepatic retention of platinum-based drugs, thereby mitigating potential hepatotoxicity risks. Serum biochemical assays further confirmed the systemic safety profile of the PLF-Cis NPs, as key hepatic and renal function markers (AST, ALT, UREA, and CREA-S levels) in the PLF-Cis NPs-treated animals remained within normal physiological ranges, with no observable signs of hepatorenal toxicity (Fig. S8). H&E staining of major organ tissues demonstrated enhanced biosafety outcomes. Compared with tumor-bearing control mice, which displayed prominent inflammatory cell infiltration in pulmonary regions, the PLF-Cis NPs group tissue exhibited histopathological features closely resembling those of control group lung tissue, with only mild and localized inflammatory responses (Fig. 7k and Fig. S9). This observation aligns with the organ distribution data, further supporting the systemic safety advantages of PLF-Cis NPs.

Tumor immune microenvironment

Single-cell Cy-TOF analysis revealed dynamic shifts in immune cell composition within tumor tissues. Through systematic profiling of cell surface marker expression (Fig. 8a), we quantified the relative abundance of distinct immune cell subsets (Fig. 8b). Notably, cytotoxic T lymphocytes (CTLs) significantly expanded in tumor-infiltrating populations, whereas myeloid-derived suppressor cells (MDSCs) markedly decreased in percentage (Fig. 8c–e). These coordinated changes in immune cell ratios collectively indicate that PLF-Cis NPs modulated the tumor immune microenvironment toward a more immunostimulatory profile.

We further performed flow cytometry to quantify tumor-infiltrating $CD4^+$ and $CD8^+$ T and DC populations in tumor tissues (Fig. 8f–j). These results demonstrated that the nonselective cytotoxicity of free cisplatin severely compromised the murine immune system. In contrast, PLF-Cis NPs markedly increased the infiltration of $CD4^+$ T cells, $CD8^+$ T cells, and mature dendritic cells (DCs) into tumors. We hypothesize that this phenomenon may be mechanistically linked to the immunogenic cell death (ICD)-inducing activity of PLF-Cis NPs.

Discussion

This study successfully established an AI-driven platform, LMCDPS, which employs a "function-oriented reverse sourcing" strategy to achieve a rational design from therapeutic goals to optimal natural raw materials. The platform's unique strength lies in its integration of dual predictive capabilities—assessing both molecular self-assembly potential and multi-target synergistic bioactivity—coupled with interpretable molecular dynamics simulations that provide mechanistic insights into the physicochemical drivers of self-assembly, thereby mitigating the "black box" limitation commonly associated with AI models in biomedical applications. Utilizing this platform, we not only efficiently identified Persimmon Leaf Flavonoids (PLF) as an ideal synergistic partner for cisplatin but also developed a self-assembled nanodrug (PLF-Cis NPs) capable of concurrently triggering apoptosis, ferroptosis, and immunogenic cell death (ICD). Notably, apoptosis and ferroptosis represent two distinct forms of regulated cell death, whereas ICD refers to an immunostimulatory phenotype associated with dying tumor cells rather than an independent death modality.

Compared to traditional self-assembled systems using single-component natural products, PLF-Cis NPs demonstrate distinct advantages. Firstly, although single-component systems are more straightforward for mechanistic deconvolution, their drug-loading capacity and pharmacological activity network are relatively limited. This study demonstrated that an AI-screened, multi-component flavonoid system can form more stable nanostructures through synergistic self-assembly with cisplatin and elicit more robust and multifaceted antitumor effects. This "many-to-one" assembly mode not only mimics the inherent multi-component synergy of natural extracts but also mitigates the potential risk of single-target action in complex biological systems. More importantly, this strategy eliminates the need for complex synthetic carriers by directly leveraging the intrinsic physicochemical properties of natural components, thereby offering favorable safety profiles, cost-effectiveness, and potential for clinical development.

PLF-Cis NPs exert their therapeutic efficacy through increased intracellular platinum accumulation and the coordinated activation of multiple cell death pathways. This is consistent with the LMCDPS-based prioritization of these flavonoids for their potential to modulate apoptosis, immune responses, and co-assembly with cisplatin, providing a functional basis for the observed multi-pathway activation. In addition to cisplatin-induced DNA damage and apoptosis, we observed that the nanoparticles induce significant lipid peroxidation accumulation, thereby driving ferroptosis. As an emerging form of regulated cell death, ferroptosis holds particular promise for addressing the common issue of cisplatin resistance in TNBC.[32] Given the complex and potentially synergistic nature of the flavonoid mixture, the contribution of individual components to this ferroptosis induction warrants further investigation. Inhibitor experiments further revealed that blocking either apoptosis or ferroptosis alone only partially rescued PLF-Cis NPs–induced cytotoxicity, suggesting that these two pathways jointly contribute to tumor cell killing. More critically, PLF-Cis NPs exhibited potent ICD induction—a feature absent in cisplatin alone[33]—likely amplified by the combined actions of apoptosis and ferroptosis. The ICD-related "eat me" signals (*e.g.*, calreticulin exposure) and damage-associated molecular patterns (*e.g.*, ATP release) successfully activated dendritic cells and promoted the infiltration of cytotoxic T cells into deep tumor regions.[34] This links con-

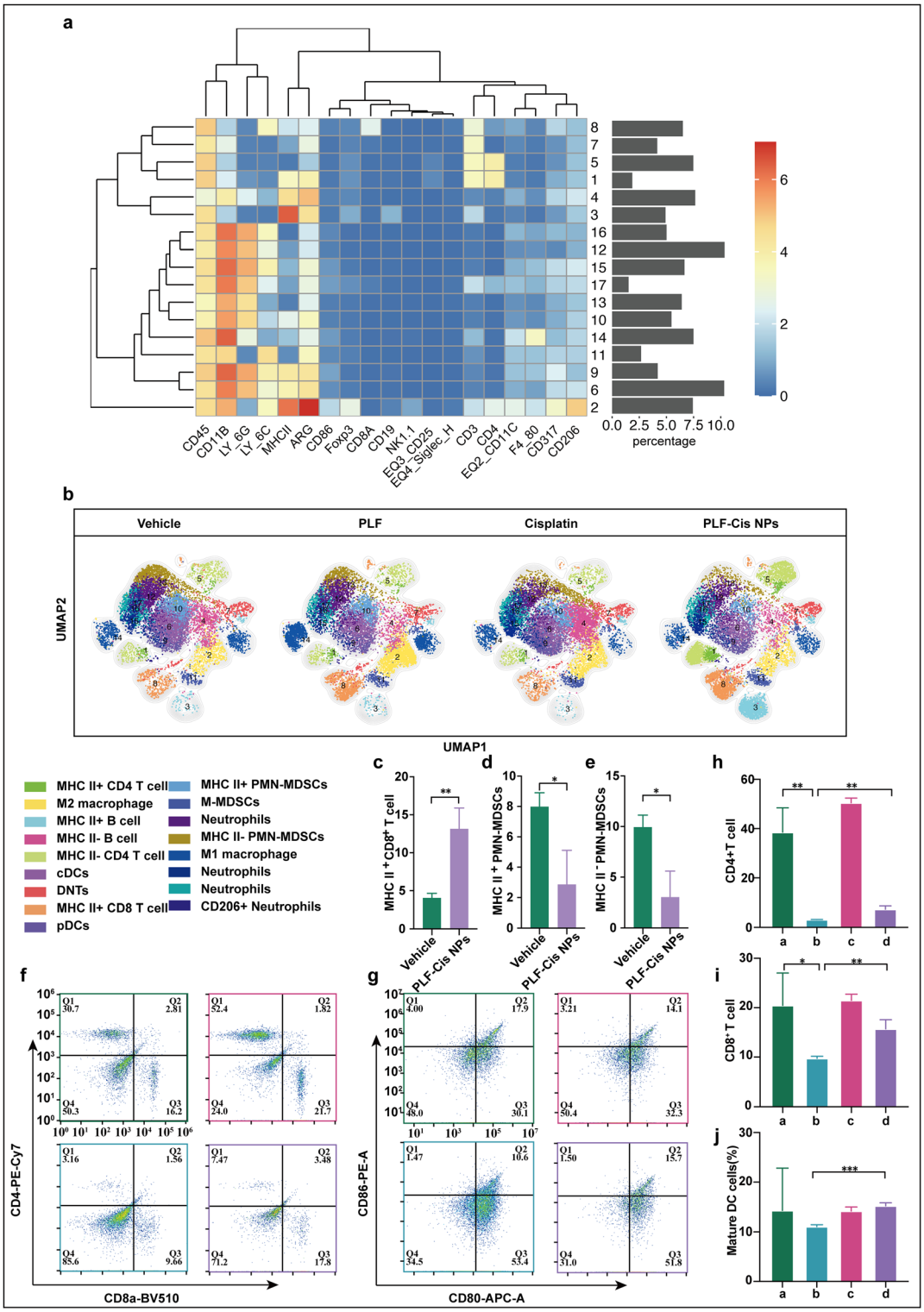

Fig. 8 Effects of the PLF-Cis NPs on the tumor immune microenvironment. (a) Expression of cell surface markers. (b) t-Distributed stochastic neighbor embedding (tSNE) plot for immune cells from tumor tissue. (c–j) DC, MDSC, and $CD4^+$ $CD8^+$ T-cell percentages in tumor tissue (a: vehicle; b: cisplatin; c: PLF; d: PLF-Cis NPs). Data are shown as mean ± SD, $n = 3$, $^*p < 0.05$, $^{**}p < 0.01$, $^{***}p < 0.001$. *ns*, not significant.

ventional cytotoxic chemotherapy with innate and adaptive immune responses, contributing to modulation of the immunosuppressive tumor microenvironment (TME).[35] Based on current understanding, redox imbalance may act as a common upstream trigger for apoptosis and ferroptosis, whereas ICD-associated DAMPs release is generally considered a down-

stream consequence of ongoing cell death. Notably, this mechanistic convergence aligns with the functional criteria used for candidate prioritization, thereby bridging computational selection with the observed multi-pathway therapeutic effects. This "chemo-immunity" synergistic effect offers a rational strategy for enhancing therapeutic efficacy against TNBC, with potential to augment anti-tumor immune responses beyond direct cytotoxicity.

Although this study presents a promising strategy, several limitations remain. First, the *in vivo* circulation behavior and pharmacokinetic properties of PLF-Cis NPs require systematic investigation, particularly their stability under physiological shear stress and dynamic blood circulation conditions, as well as their long-term biosafety in larger animal models. Second, although we observed increased expression of DAMPs and enhanced cytotoxic T cell infiltration suggestive of antitumor immune activation, the current data remain correlative and do not establish a direct causal link between ICD and T cell recruitment. Future studies will require definitive experiments to mechanistically confirm this link and assess the durability of the antitumor immune response. In parallel, the precise mechanisms by which this nanoplatform modulates the tumor immune microenvironment, as well as the balance between cisplatin's cytotoxicity and its potential immunosuppressive effects, warrant further investigation. Third, as an AI-driven platform, LMCDPS inherently relies on the quality and coverage of public database annotations, which may bias predictions toward well-characterized compounds and undervalue less-studied but potentially promising natural products. In particular, the model performance may be influenced by the chemical space represented in the training datasets, potentially favoring compounds with extensively reported structures and biological activities. Furthermore, given the inherent complexity of botanical components, the preparation process must adhere to stringent pharmaceutical standards, including purity and quality control, to minimize potential confounding factors. From a translational perspective, additional challenges should also be considered, including the scalability and batch-to-batch consistency of nanoparticle preparation, comprehensive evaluation of long-term safety, and regulatory considerations associated with complex nanomedicine systems. Addressing these issues will be essential to ensure successful downstream standardization and clinical translation. Future research will focus on these aspects to further advance the application of natural product-based self-assembled nanomedicines.

Conclusions

In summary, this study pioneers an AI-guided, rational paradigm for developing multi-component natural product-based nanodrugs. We have demonstrated that the PLF-Cis NPs, developed through AI (LMCDPS)-guided sourcing and preparation, can efficiently eliminate TNBC cells and favorably modulate the immunosuppressive TME by synergistically activating three distinct pathways—apoptosis, ferroptosis, and ICD—while exhibiting excellent antitumor efficacy and a favorable safety profile *in vivo*. This work not only provides a highly potential novel combinatorial therapy for TNBC but also represents a critical step towards modernizing natural medicine research through AI, shifting the paradigm from "empirical screening" to "rational design".

Author contributions

MT conducted the main experiments, data analysis and figure preparation. GH contributed to establish the LMCDPS platform. DZ analyzed the self-assembly mechanism. BH, MN and LC assisted with the animal experiments. YJW and YL designed this research and revised the manuscript. All authors approved the final manuscript.

Conflicts of interest

The authors declare that they have no known competing financial interests or personal relationships that could have appeared to influence the work reported in this paper.

Data availability

The supplementary data supporting this article have been included as part of the supplementary information (SI). Supplementary information is available. See DOI: https://doi.org/10.1039/d5nr05064b.

The core hyperparameters and training code of LMCDPS are consistent with those of SLCDPS and can be accessed *via* the public GitHub repository (https://github.com/geng007).

Acknowledgements

This study was supported by the National Natural Science Foundation of China for Young Scholars (No. 22407094), the Natural Science Foundation of Beijing Municipality for Young Scholars (No. 2254070), the Beijing Municipal Science & Technology Commission, Administrative Commission of Zhongguancun Science Park (Z241100009024044), the R&D Program of Beijing Municipal Education Commission (KM202410025024), and the Beijing under the CIMR Organized Scientific Research Program (CX23YZ06). This research was supported by the Research and Development Laboratory of Innovative Drugs for Metabolic Diseases of the Capital Medical University (Beijing, China), and the Central Laboratory of Capital Medical University. The graphical abstract and artworks in Figs. 3, 4 and 6 were drawn by Figdraw (https://www.figdraw.com). We specially acknowledge the late researcher Geng Hu for his invaluable contributions to model development, drug screening, and guidance on the fabrication of self-assembled nanoparticles during the early stages of this project. His dedication and expertise were indispensable.

References

1 X. Bai, J. Ni, J. Beretov, P. Graham and Y. Li, *Cancer Lett.*, 2021, **497**, 100–111.
2 D. Wang and S. J. Lippard, *Nat. Rev. Drug Discovery*, 2005, **4**, 307–320.
3 E. Jamieson and S. Lippard, *Chem. Rev.*, 1999, **99**, 2467–2498.
4 H. Li, R. Lin, Y. Zhang, Y. Zhu, S. Huang, J. Lan, N. Lu, C. Xie, S. He and W. Zhang, *Mol. Cancer*, 2024, **23**, 5.
5 L. Hu, C. Xiong, G. Wei, Y. Yu, S. Li, X. Xiong, J. J. Zou and J. Tian, *J. Colloid Interface Sci.*, 2022, **608**, 1882–1893.
6 L. Galluzzi, E. Guilbaud, D. Schmidt, G. Kroemer and F. M. Marincola, *Nat. Rev. Drug Discovery*, 2024, **23**, 445–460.
7 A. Tesniere, F. Schlemmer, V. Boige, O. Kepp, I. Martins, F. Ghiringhelli, L. Aymeric, M. Michaud, L. Apetoh, L. Barault, J. Mendiboure, J. P. Pignon, V. Jooste, P. van Endert, M. Ducreux, L. Zitvogel, F. Piard and G. Kroemer, *Oncogene*, 2010, **29**, 482–491.
8 A. P. Hernandez, A. Micaelo, R. Pinol, M. L. Garcia-Vaquero, J. J. Aramayona, J. J. Criado, E. Rodriguez, J. I. Sanchez-Gallego, A. Landeira-Vinuela, P. Juanes-Velasco, P. Diez, R. Gongora, R. Jara-Acevedo, A. Orfao, J. Miana-Mena, M. J. Munoz, S. Villanueva, A. Millan and M. Fuentes, *J. Nanobiotechnol.*, 2022, **20**, 341.
9 R. Ye, L. Sun, J. Peng, A. Wu, X. Chen, L. Wen, C. Bai and G. Chen, *J. Med. Chem.*, 2021, **64**, 3115–3130.
10 M. Davoudi, Y. Jadidi, K. Moayedi, V. Farrokhi and R. Afrisham, *J. Nanobiotechnol.*, 2022, **20**, 504.
11 Y. Liu, Y. Wang, X. Guan, Q. Wu, M. Zhang, P. Cui, C. Wang, X. Chen, X. Meng and T. Ma, *ACS Appl. Mater. Interfaces*, 2023, **15**, 26484–26495.
12 S. I. Surer, T. B. Elcitepe, D. Akcay, E. Daskin, G. C. Kocal, Z. A. Alicikus, G. Eskiizmir, K. Yapici and Y. Basbinar, *Balkan Med. J.*, 2021, **38**, 278–286.
13 J. Zhang, L. Weng, X. Su, G. Lu, W. Liu, Y. Tang, Y. Zhang, J. Wen, Z. Teng and L. Wang, *J. Colloid Interface Sci.*, 2018, **513**, 214–221.
14 X. Cheng, Z. Xie, X. Shi, Y. Huang, S. Wang, J. Li, Y. Zhang, B. Zheng and J. Liu, *Colloids Surf., B*, 2025, **256**, 115033.
15 Y. Wang, J. Zhou, L. Qiu, X. Wang, L. Chen, T. Liu and W. Di, *Biomaterials*, 2014, **35**, 4297–4309.
16 S. Dasari, S. Njiki, A. Mbemi, C. G. Yedjou and P. B. Tchounwou, *Int. J. Mol. Sci.*, 2022, **23**, 1532.
17 C. Wang, M. Zhang, J. Peng, M. Zhang, C. Lu, X. Qi, Q. Luo, Y. Wang and G. Li, *Phytomedicine*, 2024, **128**, 155504.
18 L. Galluzzi, A. Buque, O. Kepp, L. Zitvogel and G. Kroemer, *Nat. Rev. Immunol.*, 2017, **17**, 97–111.
19 K. H. Bae, S. Tan, A. Yamashita, W. X. Ang, S. J. Gao, S. Wang, J. E. Chung and M. Kurisawa, *Biomaterials*, 2017, **148**, 41–53.
20 G. Yamankurt, E. J. Berns, A. Xue, A. Lee, N. Bagheri, M. Mrksich and C. A. Mirkin, *Nat. Biomed. Eng.*, 2019, **3**, 318–327.
21 I. Iqbal, M. Younus, K. Walayat, M. U. Kakar and J. Ma, *Comput. Med. Imaging Graph.*, 2021, **88**, 101843.
22 W. Pan, G. Hu, S. Li, G. Li, X. Feng, Z. Wu, D. Zhang, L. Qin, X. Wang, L. Hu, J. Xu, L. Hu, Y. Jia, X. Wen, J. Wang, C. Zhang, J. Zhou, W. Li, X. Wang, Y. Wang and S. Wang, *Sci. Bull.*, 2023, **68**, 838–850.
23 J. U. Becker, D. Mayerich, M. Padmanabhan, J. Barratt, A. Ernst, P. Boor, P. A. Cicalese, C. Mohan, H. V. Nguyen and B. Roysam, *Kidney Int.*, 2020, **98**, 65–75.
24 Z. Zhang, W. Du, X. Zhang, H. Cui, B. Cheng, X. Han, K. He, T. Yin, X. Liu, N. Xian, Z. Wang, M. Liu, D. Han, J. Liu, Y. Zheng and Y. Wang, *Adv. Sci.*, 2025, e12422.
25 P. Rasoanaivo, C. W. Wright, M. L. Willcox and B. Gilbert, *Malar. J.*, 2011, **10**, S4.
26 N. E. Thomford, D. A. Senthebane, A. Rowe, D. Munro, P. Seele, A. Maroyi and K. Dzobo, *Int. J. Mol. Sci.*, 2018, **19**, 1578.
27 B. Moreno-Chamba, J. Salazar-Bermeo, M. Narvaez-Asensio, P. Navarro-Simarro, D. Saura, M. Neacsu, N. Marti, M. Valero and M. C. Martinez-Madrid, *Phytomedicine*, 2024, **134**, 156020.
28 B. Moreno-Chamba, J. Salazar-Bermeo, M. C. Martínez-Madrid, V. Lizama, F. Martín-Bermudo, G. Berná, M. Neacsu, D. Saura, N. Martí and M. Valero, *LWT – Food Sci. Technol.*, 2022, **156**, 113011.
29 F. Ding, L. Zhang, H. Chen, H. Song, S. Chen and H. Xiao, *Nanoscale Horiz.*, 2020, **5**, 999–1015.
30 S. Jahan, M. E. Karim and E. H. Chowdhury, *Biomedicines*, 2021, **9**, 114.
31 M. Lv, Y. Zheng, X. Dai, J. Zhao, G. Hu, M. Ren, Z. Shen, Z. Su, C. Wu, H. K. Liu, X. Xue and Z. W. Mao, *J. Med. Chem.*, 2024, **67**, 20156–20171.
32 M. Ni, J. Zhou, Z. Zhu, Q. Xu, Z. Yin, Y. Wang, Z. Zheng and H. Zhao, *Phytomedicine*, 2023, **112**, 154701.
33 S. V. Hato, A. Khong, I. J. de Vries and W. J. Lesterhuis, *Clin. Cancer Res.*, 2014, **20**, 2831–2837.
34 L. J. Yang, T. Han, R. N. Liu, S. M. Shi, S. Y. Luan and S. N. Meng, *Biomed. Pharmacother.*, 2024, **177**, 117099.
35 L. Song, Y. Hao, C. Wang, Y. Han, Y. Zhu, L. Feng, L. Miao and Z. Liu, *J. Controlled Release*, 2022, **350**, 922–932.